

PAPER

## $\alpha$ -Fe<sub>2</sub>O<sub>3</sub>-based artificial synaptic RRAM device for pattern recognition using artificial neural networks

To cite this article: Prabana Jetty *et al* 2023 *Nanotechnology* **34** 265703

View the [article online](#) for updates and enhancements.

### You may also like

- [Emerging memory technologies for neuromorphic computing](#)  
Chul-Heung Kim, Suhwan Lim, Sung Yun Woo et al.
- [Synaptic plasticity investigation in permalloy based channel material for neuromorphic computing](#)  
P Monalisha, Shengyao Li, Tianli Jin et al.
- [A multilevel electrolyte-gated artificial synapse based on ruthenium-doped cobalt ferrite](#)  
P Monalisha, Shengyao Li, Tianli Jin et al.

**PRIME**  
PACIFIC RIM MEETING  
ON ELECTROCHEMICAL  
AND SOLID STATE SCIENCE

HONOLULU, HI  
Oct 6-11, 2024

Abstract submission deadline:  
**April 12, 2024**

Learn more and submit!

**Joint Meeting of**  
The Electrochemical Society  
•  
The Electrochemical Society of Japan  
•  
Korea Electrochemical Society

# $\alpha$ -Fe<sub>2</sub>O<sub>3</sub>-based artificial synaptic RRAM device for pattern recognition using artificial neural networks

Prabana Jetty<sup>1</sup>, Kannan Udaya Mohanan<sup>2</sup>  and S Narayana Jammalamadaka<sup>1,\*</sup> 

<sup>1</sup>Magnetic Materials and Device Physics Laboratory, Department of Physics, Indian Institute of Technology Hyderabad, Hyderabad, 502 284, India

<sup>2</sup>Department of Electronic Engineering, Gachon University, Seongnam-si, Gyeonggi-do, 13120, Republic of Korea

E-mail: [surya@phy.iith.ac.in](mailto:surya@phy.iith.ac.in)

Received 7 December 2022, revised 21 March 2023

Accepted for publication 28 March 2023

Published 12 April 2023



## Abstract

We report on the  $\alpha$ -Fe<sub>2</sub>O<sub>3</sub>-based artificial synaptic resistive random access memory device, which is a promising candidate for artificial neural networks (ANN) to recognize the images. The device consists of a structure Ag/ $\alpha$ -Fe<sub>2</sub>O<sub>3</sub>/FTO and exhibits non-volatility with analog resistive switching characteristics. We successfully demonstrated synaptic learning rules such as long-term potentiation, long-term depression, and spike time-dependent plasticity. In addition, we also presented off-chip training to obtain good accuracy by backpropagation algorithm considering the synaptic weights obtained from  $\alpha$ -Fe<sub>2</sub>O<sub>3</sub> based artificial synaptic device. The proposed  $\alpha$ -Fe<sub>2</sub>O<sub>3</sub>-based device was tested with the FMNIST and MNIST datasets and obtained a high pattern recognition accuracy of 88.06% and 97.6% test accuracy respectively. Such a high pattern recognition accuracy is attributed to the combination of the synaptic device performance as well as the novel weight mapping strategy used in the present work. Therefore, the ideal device characteristics and high ANN performance showed that the fabricated device can be useful for practical ANN implementation.

Supplementary material for this article is available [online](#)

Keywords: memristor device, RRAM, potentiation, depression, artificial neural networks, spike time-dependent plasticity

(Some figures may appear in colour only in the online journal)

## Introduction

Neuromorphic computing has emerged to give solutions to the 'Big Data' pertinent to unstructured data formats such as characters, images, and sounds those experiencing challenges by current computing technology based on Von-Neumann architecture [1, 2]. It is brain-inspired computing and consists of advantages such as complex operations, massive parallelism, in-memory computing, and structural plasticity [3]. The brain consists of  $\sim 10^{11}$  neurons and  $\sim 10^{15}$  synapses which

receive signals in the form of action potentials from other neurons and the transfer of signals is enabled by synapses [4, 5]. A synapse is a two-terminal transmission line between pre-synaptic input (axon firing spikes) and post-synaptic output (dendrite receiving the transmitters) [6]. Therefore, novel devices have been developed to mimic the behaviour of biological elements of the neural network, such as spiking neurons and learning process [7, 8].

Among various synaptic memory devices, resistive random access memory (RRAM)-based synapses consist simple architecture with CMOS compatibility [9]. Electronically one can control conductance of RRAM synapses similar to neural

\* Author to whom any correspondence should be addressed.

spikes, which causes potentiation and depression of a biological synapse [10, 11]. The change in synaptic weight of biological synapses can be seen as a change in conductance (resistance states) of artificial synapses based on RRAM devices. It has been believed that change in resistance of these devices is due to formation and rupturing of 1D filaments those are made by oxygen vacancies up on application of external electric field. [12]. The process of tuning the synaptic RRAM device from HRS to LRS is termed as a SET process, while the process of tuning RRAM from LRS to HRS is known as the RESET process [12, 13]. Synaptic RRAM devices show some similarities with biological synapses and has been demonstrated to emulate various synaptic functions such as long-term potentiation (LTP), long-term depression (LTD), and spike time-dependent plasticity (STDP) [14–17]. The synaptic weights of LTP and LTD are used for software training in Artificial neural network (ANN). The neuromorphic research has focused on aiming the development of ANNs for high-accurate recognition of image, video, and audio data [18]. ANNs are complex systems and connected with artificial ‘neurons’ to perform various computational tasks. These neurons are interconnected with each other via ‘synapses’, which can be assigned a weight to modulate the strength of an input being received by a neuron [19]. To achieve this, such networks are generally organized into layers including an input layer, intermediate hidden layers, and an output layer, where each layer is composed of a number of nodes to allow for data processing [20]. In the training phase, the weights of the ANN are adjusted to yield a high train accuracy. Once the training is completed, the final test accuracy is obtained by evaluating the ANN’s performance on the test dataset.

RRAMs have been demonstrated as a neuromorphic synaptic memristor device with different switching materials such as  $\text{WO}_x$  [21],  $\text{HfO}_x$  [22],  $\text{TaO}_x$  [23],  $\text{MoO}_x$  [24],  $\text{InGaZnO}$  [25],  $\text{RGO}+\text{chitosan}$  [26],  $\text{TiO}_2$  [27] and Graphene oxide [28] respectively. Apart from the above, iron (Fe) is an inexpensive material as it is the fourth element in the Earth’s crust. On the other hand,  $\text{Fe}_2\text{O}_3$  is stable and has been utilized in diverse applications ranging from medicine, electronics, metallurgy, automotive sector, building construction, energy, textiles and art [29, 30]. Earlier, Xiaobing Yan *et al* has proved change in resistive switching model of  $\alpha\text{-Fe}_2\text{O}_3$  by electroforming in the films [31]. Digital switching with high performance and low power consumption have been demonstrated on  $\text{Ag}/\text{Fe}_2\text{O}_3/\text{FTO}$ -based RRAM device [32]. Yet in another study, Xian Wan *et al* have reported a Biomimicked atomic-layer-deposited iron oxide-based memristor with synaptic potentiation and depression functions [33]. Changhong Wang *et al* have investigated the effect of the compliance current on the analog behaviour of the device using the  $\text{Pt}/\text{FeO}_x/\text{Pt}$  structure [34]. In this work, we demonstrate neuronal functionalities such as (a) long-term potentiation (LTP) (b) long-term depression (LTD) (c) spike time-dependent plasticity (STDP) of  $\alpha\text{-Fe}_2\text{O}_3$  based artificial synapse. In addition, we also present off chip training to obtain good accuracy by backpropagation algorithm considering the synaptic weights obtained from  $\alpha\text{-Fe}_2\text{O}_3$  based

artificial synaptic RRAM device for FMNIST data set using ANNs.

## Experiments

The RRAM device with a structure of  $\text{Ag}/\alpha\text{-Fe}_2\text{O}_3/\text{Fluorine doped tin oxide (FTO)}$  was fabricated to establish resistive switching (RS) characteristics. Prior to the device fabrication, the substrate FTO was cleaned by the ultra-sonication process with deionized water, acetone, and 2-propanol individually. The iron-thin films were deposited using a thermal evaporator (make advanced processing technology (APT)). The base vacuum pressure was  $7.5 \times 10^{-6}$  mbar and during the deposition, the operating pressure was  $1.8 \times 10^{-5}$  mbar. The power applied to the target boat for the iron to evaporate was 196.5 Watts. The deposited iron (Fe) films on the FTO substrate were annealed at  $400^\circ\text{C}$  in a box furnace for four hours to oxidize Fe films. The cross-sectional imaging and the thickness of the thin film was determined using scanning electron microscope (SEM) and found  $0.87 \mu\text{m}$  as thickness of  $\alpha\text{-Fe}_2\text{O}_3$ . Image pertinent to SEM shown in supporting information (figure S1). Then silver conducting epoxy was used as a top electrode. The diameter of top electrode is 0.5 mm, while, the distance between two electrodes is 3 mm. The resistance of FTO is approximately  $15 \Omega$ . The crystalline phase of the thin films was determined using Rigaku smart lab SE x-ray diffractometer. The phase purity of the  $\alpha\text{-Fe}_2\text{O}_3$  thin film is confirmed with the grazing incidence x-ray diffraction (GI-XRD) with a grazing angle of  $0.5^\circ$  and  $2\theta$  range of  $10^\circ - 80^\circ$ . Indeed, such graph is shown in the supporting information (figure S2). The electrical measurements were carried out using Keithley 4200 SCS semiconductor characterization system with a current compliance of 7 mA for  $\text{Ag}/\alpha\text{-Fe}_2\text{O}_3/\text{FTO}$  device respectively. During our measurements, a negative bias voltage was applied to Ag top electrode and positive bias to the bottom FTO electrode in the current perpendicular to the plane (CPP) configuration. Pulsed  $I-V$  characteristics were performed using Keithley 4200 SCS and are shown in figures 3(a) and (c) by applying continuous pulses with pulse amplitude of 1 V and pulse width of  $150 \mu\text{s}$ . For the image recognition, the training is performed -on FMNIST data set of 60 000 images and test dataset of 10 000 images. This database is widely used for training and testing in the field of machine learning and image processing.

Figure 1(a) shows the schematic diagram of fabricated  $\text{Ag}/\alpha\text{-Fe}_2\text{O}_3/\text{FTO}$ - based synaptic RRAM device. Figure 1(b) reveals the  $I-V$  characteristics of  $\text{Ag}/\alpha\text{-Fe}_2\text{O}_3/\text{FTO}$  device in logarithmic scale respectively. Initially, we tried to develop the RS in the device. Here FTO acts as the bottom electrode and silver as the top electrode and  $\alpha\text{-Fe}_2\text{O}_3$  acts as an active layer. The current perpendicular to the plane (CPP) configuration was used to perform  $I-V$  characteristics in the device. The electrical measurements were carried out under ambient conditions (300 K) and at the current compliance of 7 mA to prevent dielectric breakdown. A DC sweeping voltage of +2.3 to  $-1.6$  V was applied to measure the  $I-V$  response of the device. The device showed

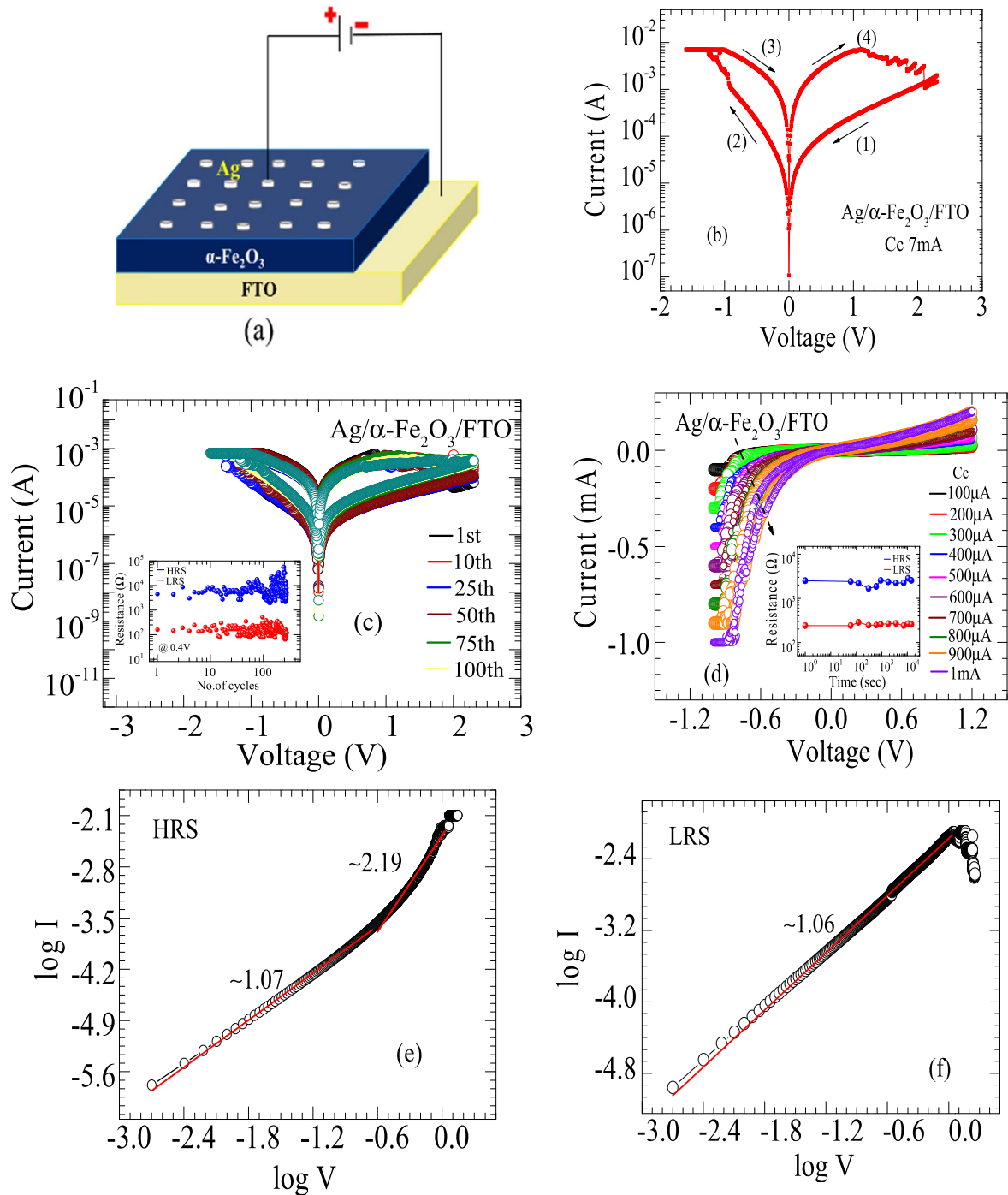


**Figure 1.** (a) Schematic diagram of fabricated Ag/ $\alpha$ -Fe<sub>2</sub>O<sub>3</sub>/FTO device where fluorine doped tin oxide (FTO) was used as bottom electrode and Ag as top electrode. (b)  $I$ - $V$  characteristics of Ag/ $\alpha$ -Fe<sub>2</sub>O<sub>3</sub>/FTO device with compliance current of 7 mA (c)  $I$ - $V$  characteristics of the device with different laps under single logarithmic coordinates. Inset figure shows the endurance characteristics up to 150 cycles. (d) Multilevel resistance switching under different compliance current. Inset figure shows the retention characteristics of RRAM device up to  $1.49 \times 10^4$  s. Double logarithmic scale for  $I$ - $V$  curve indicate (e) Trap controlled SCLC mechanism for HRS state and (f) Ohmic conduction for LRS state.

reversible analog bipolar resistive switching where SET is taking place at  $-1.2$  V and RESET at  $+2.1$  V. The arrow marks on the  $I$ - $V$  characteristics indicate the direction of the voltage sweep that we used during the measurements. Figure 1(c) shows a stable analog switching performance for nearly for 100 cycles. The inset graph of figure 1(c) indicates the endurance characteristics of the device, which hints that

the device is stable up to 275 cycles with a switching window of 10. Indeed, such a switching window is sufficient to distinguish HRS and LRS. Figure 1(d) shows DC  $I$ - $V$  bipolar switching curves of Ag/ $\alpha$ -Fe<sub>2</sub>O<sub>3</sub>/FTO-based synaptic RRAM device for different compliance currents. It is evident from figure that multistage compliance prevails by changing the compliance current from  $100 \mu\text{A}$  to  $1\text{mA}$ . We observe the

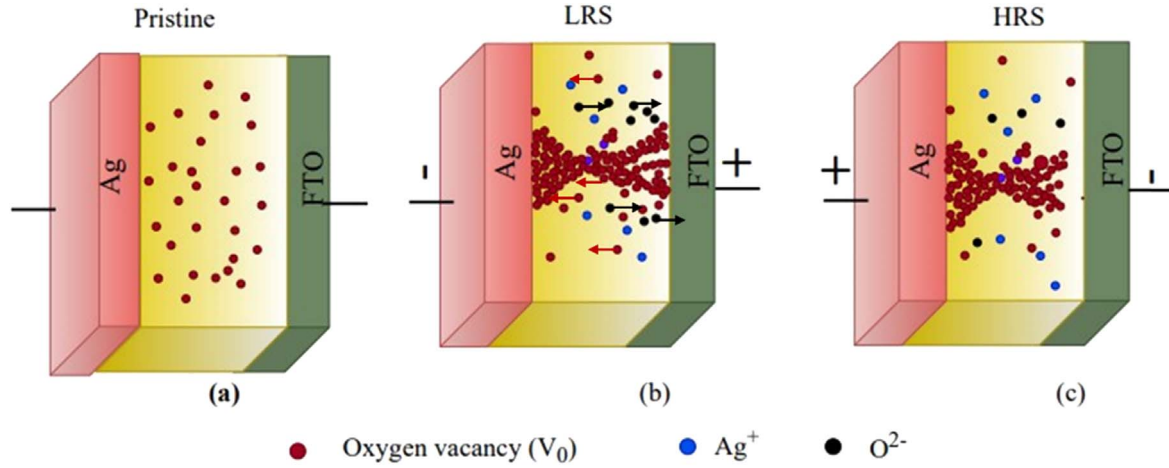


**Figure 2.** Schematic to demonstrate (a) Oxygen defects in Ag/ $\alpha$ -Fe<sub>2</sub>O<sub>3</sub>/FTO based device. (b) the formation of conductive filaments due to oxygen defects when negative bias is applied to top electrode and positive bias to bottom electrode in Ag/ $\alpha$ -Fe<sub>2</sub>O<sub>3</sub>/FTO device. (c) Rupturing of the filament when the polarity of voltage changed in Ag/ $\alpha$ -Fe<sub>2</sub>O<sub>3</sub>/FTO device.

gradual increase in conductance with an increase in compliance current as shown in figure 1(d), which is suitable for neuromorphic applications. Inset figure 1(d) represents retention characteristics of the Ag/ $\alpha$ -Fe<sub>2</sub>O<sub>3</sub>/FTO device. From the figure it is evident that the device consists good retentivity up to  $1.49 \times 10^4$  s. The power consumed to operate the present device is found to be 8 mW.

Several models have been sought to interpret the resistive switching phenomenon in oxide materials including  $\ln I \propto \ln V$  (space-charge limited current, or (SCLC)) [35],  $\ln I/V \propto 1/V$  (Fowler–Nordheim tunneling) [36],  $\ln I/V \propto \sqrt{V}$  (Poole–Frenkel emission) [37],  $\ln I \propto \sqrt{V}$  (Schottky emission) [38]. In order to investigate the electron transport mechanism, the HRS and LRS states are plotted in a double logarithmic scale shown in figures 1(e) and (f). As depicted in figure 1(e), the HRS of Ag/ $\alpha$ -Fe<sub>2</sub>O<sub>3</sub>/FTO is fitted well with a space charge limited conduction mechanism (SCLC). The HRS is divided into two regions based on the slopes. At the lower voltage region, the slope is equal to  $\sim 1.07$  ( $J \propto V$ ) as shown in figure 1(e). Indeed, this is typical for the ohm's law and corresponding equation can be expressed as [39–44]

$$J_{\text{ohm}} = \frac{qn\mu_n V}{d}, \quad (1)$$

where  $q$  is the electronic charge,  $n = N_c e^{-\frac{(E_c - E_f)}{kT}}$  is the free electron concentration inside the layer;  $N_c = 2 \left( \frac{2\pi m^* kT}{h^2} \right)^{\frac{3}{2}}$  is the effective density of states of electron in the conduction band,  $k$  is the Boltzmann constant;  $m^*$  is the electron effective mass,  $h$  is the Planck's constant;  $\mu_n$  is the electron mobility;  $d$  is the thickness of switching layer. Therefore, at low voltage region the current is dominated by free carriers. At higher voltage region the slope is  $\sim 2.19$ . If the applied voltage is higher than the transition voltage ( $V_{\text{tr}}$ ) it follows trap-filled limit voltage ( $V_{\text{TFL}}$ ) and can be expressed as [40, 45]:

$$J_{\text{SCLC}} = \frac{9}{8} \varepsilon \varepsilon_0 \mu_n \theta \frac{V^2}{d^3}, \quad (2)$$

where  $\varepsilon$  is the switching layer dielectric constant,  $\varepsilon_0$  is the vacuum permittivity,  $\theta = \left( \frac{N_c}{N_t} \right) e^{-\frac{(E_c - E_t)}{kT}}$  is the free charge carrier fraction of all integrated carriers (free and trapped), and  $N_t$  is the trap density,  $E_c - E_t$  is the electron trap depth. Over here,  $\varepsilon$  and  $\theta$  are the static dielectric constant and the ratio of the free carrier density to all carriers respectively. After all the traps are filled by the injected charge carriers, current increases rapidly which shows Ohmic behaviour in LRS with a slope  $\sim 1.06$  as shown in figure 1(f) that represents the transition from HRS to LRS.

Now we discuss the conceivable mechanism that explains the origin of the RS in the present device. Figure 2 represents the schematic diagram to explain the RS mechanism in Ag/ $\alpha$ -Fe<sub>2</sub>O<sub>3</sub>/FTO device. Initially, the device is in HRS, where the defects are distributed homogeneously as shown in figure 2(a). For the Ag/ $\alpha$ -Fe<sub>2</sub>O<sub>3</sub>/FTO when a negative bias is applied to the top electrode and a positive bias to the bottom electrode, the oxygen ions are pulled towards the bottom electrode shown by the arrow in figure 2(b). Indeed, this leads to generation of the oxygen vacancies. These oxygen vacancies gather and form 1D conduction channels as shown in figure 2(b). When the polarity changes, rupturing of the filaments take place and HRS state can be obtained as shown in figure 2(c).

From figure 3, it is clear that there exists analog switching in the Ag/ $\alpha$ -Fe<sub>2</sub>O<sub>3</sub>/FTO synaptic device, which may be useful for neuromorphic computing. To realize whether the device is suitable for the neuromorphic computing it is crucial to explore and demonstrate synaptic learning rules such as (a) LTP, (b) LTD and (c) STDP. To mimic this functionality in Ag/ $\alpha$ -Fe<sub>2</sub>O<sub>3</sub>/FTO device, single and sequentially triggered pulses are applied to the top electrode. The conductance of the device enhances or diminishes depending on the amplitude and duration of the applied pulse. The conductance of  $\alpha$ -Fe<sub>2</sub>O<sub>3</sub> is equivalent to the synaptic weight of the biological synapse. When a negative pulse with an amplitude of  $V_{\text{set}} = -1$  V and pulse width of 150  $\mu$ s of 80 pulses (figure 3(a)) is applied to the top electrode of the

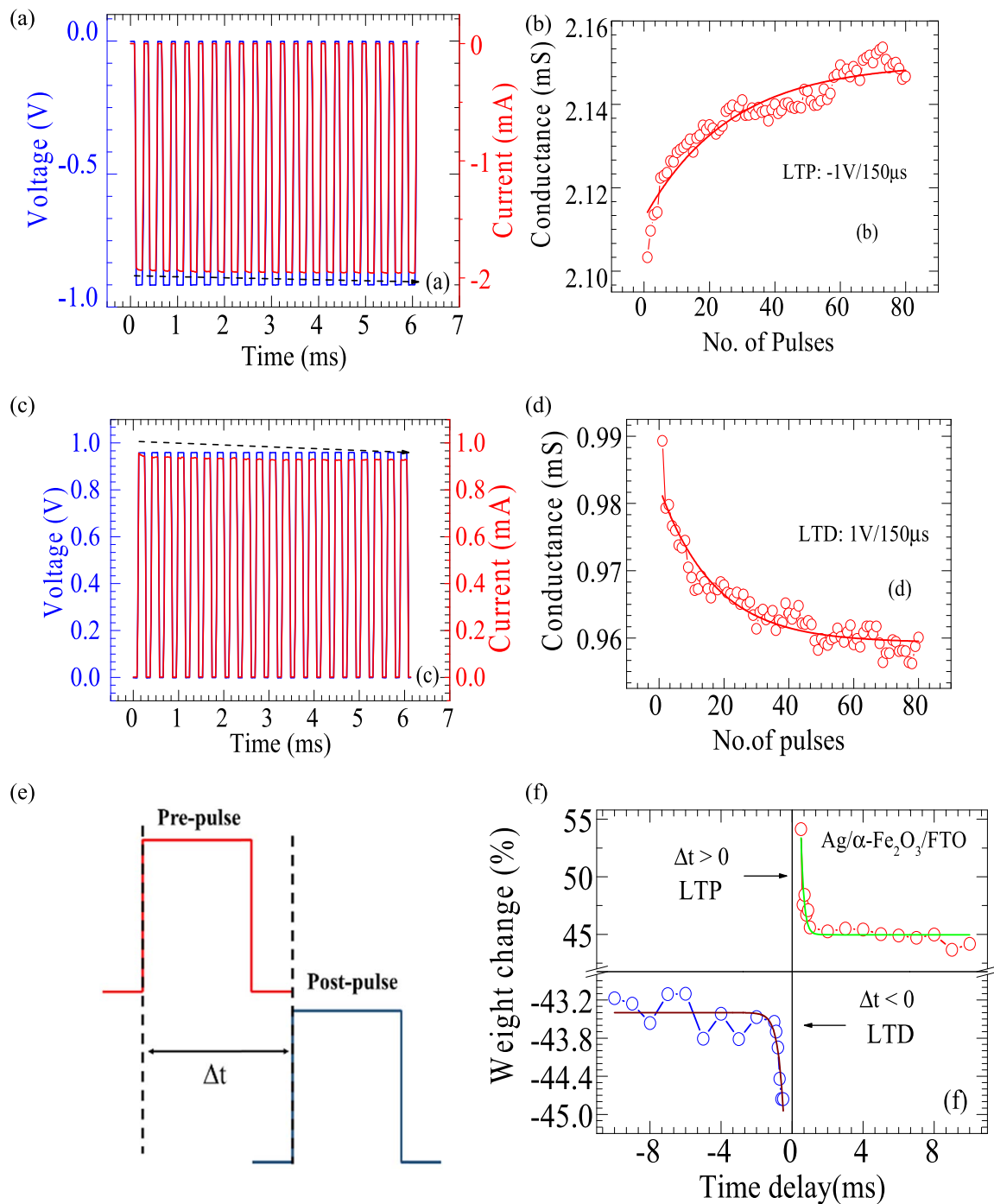


**Figure 3.** (a) Conductance modulation by applying a constant negative pulse amplitude of  $-1$  V with pulse width  $150 \mu\text{s}$  (b) Gradual SET process indicating LTP characteristics. (c) Conductance modulation by applying positive pulse  $+1$  V with a pulse width of  $150 \mu\text{s}$ . (d) Gradual RESET process, which indicates LTD characteristics. (e) Schematic presentation of STDP setup and pulse used for the experiment. (f) STDP characteristics of the device that shows the relationship between time delay with synaptic weight change.

device, the conductance of the Ag/ $\alpha$ -Fe<sub>2</sub>O<sub>3</sub>/FTO increases as shown in figure 3(b), which represents the LTP. On the other hand, by applying a positive pulse with an amplitude of  $V_{\text{reset}} = +1$  V and pulse width of  $150 \mu\text{s}$  of 80 pulses (figure 3(c)) the conductance decreases as shown in figure 3(d) which represents the LTD. These both LTP and LTD plots are fitted with exponential functions. Apart from the above, we also investigated the pulse training

performances as a function of pulse amplitude from  $-0.8$  to  $-1.6$  V with a fixed pulse width of  $150 \mu\text{s}$  for LTP and  $+0.8$  to  $+1.6$  V for LTD shown in supporting information (figure S3.)

Furthermore, we have investigated the STDP rule which is another important learning rule in the neural system. It is the relationship between change of synaptic weight ( $\Delta w$ ) and time interval ( $\Delta t$ ) that results from activity variations of the

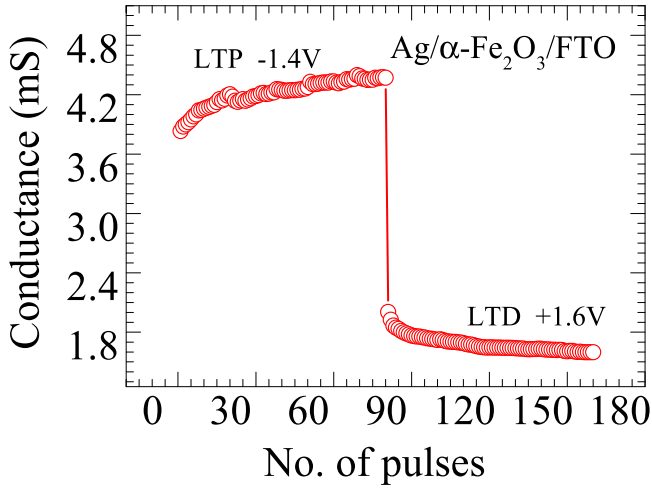


**Figure 4.** Shows the synaptic weights of Long-term potentiation (LTP) at  $-1.4$  V and long-term depression (LTD) at  $+1.6$  V.

pre- and post-neurons [46, 47]. The change in conductance or weight (%) is calculated using formula [28]

$$\Delta G = \frac{G_{\text{after}} - G_{\text{before}}}{G_{\text{before}}},$$

$G_{\text{before}}$  is the conductance before pre- and post—spike pairs and  $G_{\text{after}}$  is the conductance after pre-and post- spikes. Obviously for an RRAM device top and bottom electrodes are compared to pre-and post- synaptic neurons and pulses applied on to the electrode can mimic spikes by biological synapse. The schematic of applied pre-and post- pulses of pulse amplitude 1 V with time delay of 1 ms is shown in figure 3(e). The STDP characteristics of Ag/ $\alpha$ -Fe<sub>2</sub>O<sub>3</sub>/FTO synaptic device are shown in figure 3(f). From the figure 3(f), it is clear that when  $\Delta t (= t_{\text{pre}} - t_{\text{post}}) > 0$  or as the relative timing between pre and post pulse decreases, there is an increase in weight change ( $\Delta W$ ), which proves the enhancement in the conductance that represents potentiation. On the other hand, when  $\Delta t < 0$  or relative timing between pre and post pulses increases,  $\Delta W$  decreases, mimics the depression behaviour. Based on the above results, it can be concluded that Ag/ $\alpha$ -Fe<sub>2</sub>O<sub>3</sub>/FTO based synaptic device shows STDP behaviour by changing the time delay between pre and post synaptic pulses. Indeed, the behaviour mimics the biological synapses.

In order to evaluate the neuromorphic learning capability of the fabricated synaptic device based on Ag/ $\alpha$ -Fe<sub>2</sub>O<sub>3</sub>/FTO, the variation of the conductance pertinent to LTP and LTD recorded and is shown in figure 4. Over here, the conductance is used as synaptic weight elements for a simulated image recognition task. We designed a single hidden layer ANN based on the Fashion Modified National Institute of Standards and Technology (FMNIST) dataset [48] for off-chip image recognition task [49]. Figure 5(a) shows the schematic structure of the ANN for identification of a sample image from the FMNIST dataset. The ANN consists of 784 input neurons (linearized  $28 \times 28$  FMNIST patterns), 512 hidden neurons and 10 output neurons. All the ANN simulations are implemented using the open source Pytorch package [50].

The FMNIST dataset consists of  $28 \times 28$  grayscale images of fashion articles grouped into 10 categories. The training dataset has 60 000 images and the test dataset has 10 000 images. We used a mini-batch stochastic gradient descent (SGD) algorithm [51] for the weight update after each epoch during the ANN training process. The rectified linear unit (ReLU) function was the activation function, and the mean cross-entropy loss function is used for calculating the loss during the ANN training process. We use a total of 100 epochs for the training process where each epoch corresponds to one full pass of the training data and its subsequent evaluation on test data. Table 1 depicts the list of Hyperparameters and their names/ values that we used for ANN simulations.

After the ANN training, we adapt a post-training quantization procedure for the inference process. The trained software weight values ( $W_{sw}$ ) are scaled to the range of absolute device conductance values ( $G$ ) extracted from the LTP/LTD characteristics exist in figure 4. The scaling equation [52] is given as:

$$G_{fn} = W_{sw} \times \frac{G_m}{W_m} + \delta G, \quad (3)$$

Here,  $G_{fn}$  denotes the scaled conductance value to be introduced into the hardware sense synaptic array.  $W_m$  represents the maximum software trained weight for the particular hidden layer whereas  $G_m$  represents the maximum device conductance value. The error term  $\delta G$  incorporates the various synapse array errors like conductance drift, cycle-to-cycle conductance changes etc. In fact, we have used a mean of zero and a standard deviation of one for sampling the  $\delta G$  values [52]. The conductance distribution of our device follows a Gaussian distribution as shown in the figure S4 (supporting information). The maximum standard deviation for our measured LTP/LTD determined to be close to 0.75 mS. Taking into account any further measurement errors or non-idealities like the device-to-device variation, we have chosen an upper limit of 1 mS as the standard deviation for our simulations.

Since the device conductance values are only positive, a differential conductance pair [15] with opposite polarity ( $G_{fn}^+$  and  $G_{fn}^-$ ) are used to map the positive and negative weights to the hardware sense synaptic array to improve simulation convergence

$$G_{fn}^i = G_{fn}^+ - G_{fn}^-. \quad (4)$$

The as-mapped differential pair device conductance values are subsequently used for the inference task. Figure 5(b) shows the FMNIST image recognition accuracy evolution during the training process. We observe that the device-based ANN records a high-test accuracy of 88.06% on the FMNIST image recognition task. This is comparable to the purely software-based ANN test accuracy of 88.8%. We also studied the effect of quantized weight levels on the image recognition performance of the synaptic device. Weight quantization [53] is an important consideration in designing compact neuromorphic hardware especially for inference applications like face recognition, smart sensors etc. From the

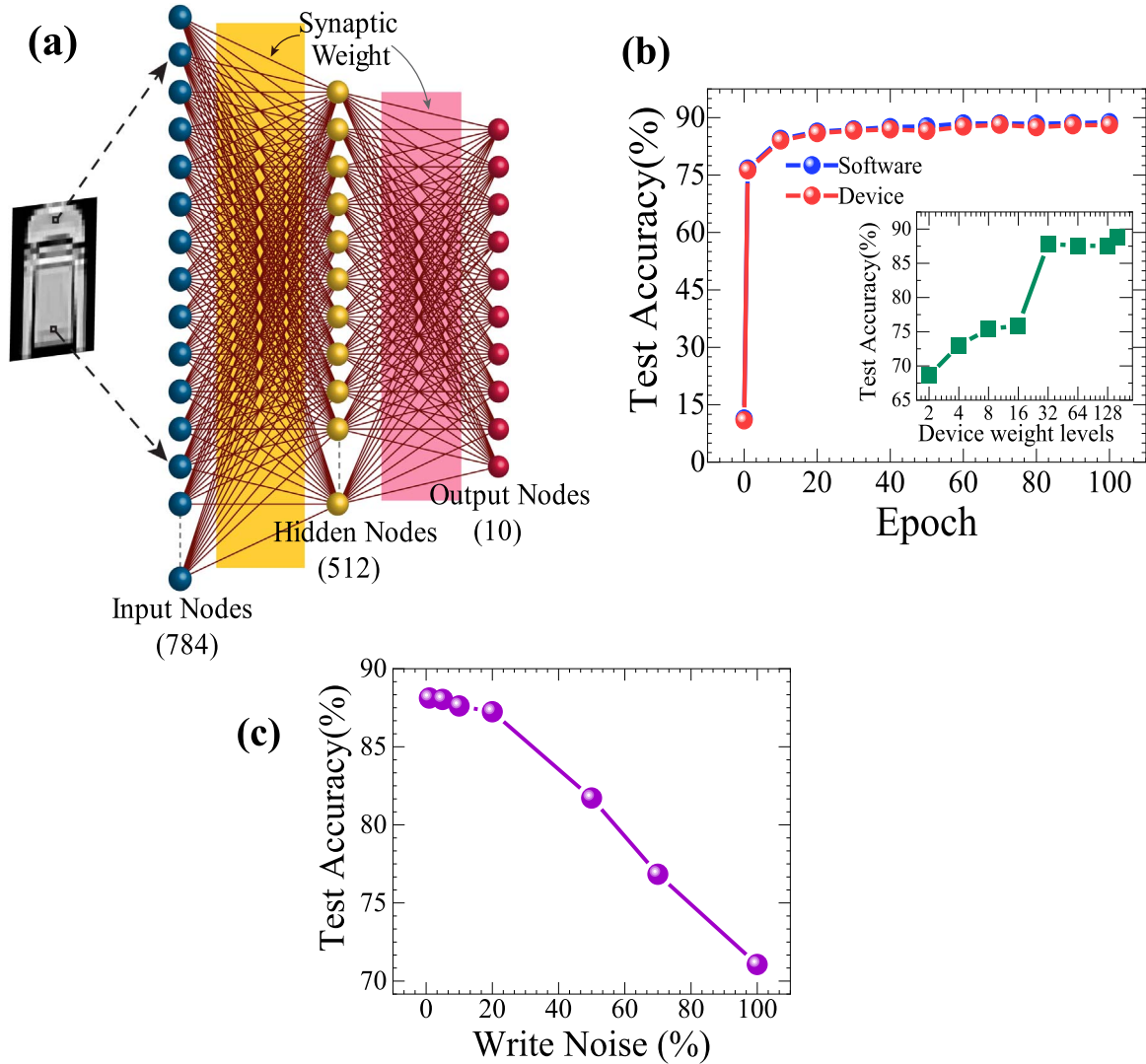


**Figure 5.** (a) Illustration of the artificial neural network (ANN) used for the FMNIST image recognition (b) Test accuracy (%) evolution during the training process with respect to the number of epochs. Blue curve depicts the fully software-based implementation whereas the red curve depicts the synaptic device  $\text{Ag}/\alpha\text{-Fe}_2\text{O}_3/\text{FTO}$  based ANN. Inset shows the test accuracy (%) dependence on the number of quantized device weights levels (c) Test accuracy (%) variation with the write noise (%).

**Table 1.** Hyperparameters and their names/ values that we used for Artificial neural network (ANN) simulations.

Hyperparameter	Name/Value
Batch size	32
Learning rate	0.01
Bias	No
Training epochs	100
Activation function	Rectified linear unit (ReLU)
Loss function	Cross entropy loss
Optimiser	Stochastic gradient descent
Number of nodes in Hidden layer	512

inset of figure 5(b), we observe that a high image recognition accuracy of  $\sim 88\%$  is retained with 5 bit ( $2^5 = 32$  levels) weight quantitation below which there is a sharp drop in accuracy. However, it is also interesting to note that the synaptic device-based ANN retains a test accuracy of greater

than 68% for the highly quantized 2 bit weights. Weight values mapped to synaptic arrays are prone to write noise which adversely affects the synaptic device performance for pattern recognition. Hence, we have tested the performance of the device-based ANN after incorporating write noise in the mapped conductance values obtained from equation (2). Write noise has been calculated as percentage random noise in proportion to the actual mapped weight value. From figure 5(c), we clearly observe that the test accuracy remains above 85% till a relatively high write noise of 20%. Such a high write noise resilience is advantageous for the practical neuromorphic hardware realization.

To further evaluate the performance of our synaptic device-based ANN, we have used the confusion matrix for understanding the capability of the ANN towards output class distinction. The confusion matrix for the synaptic device based ANN figure 6(a) shows a high value along the main diagonal axis which shows the number of normalized



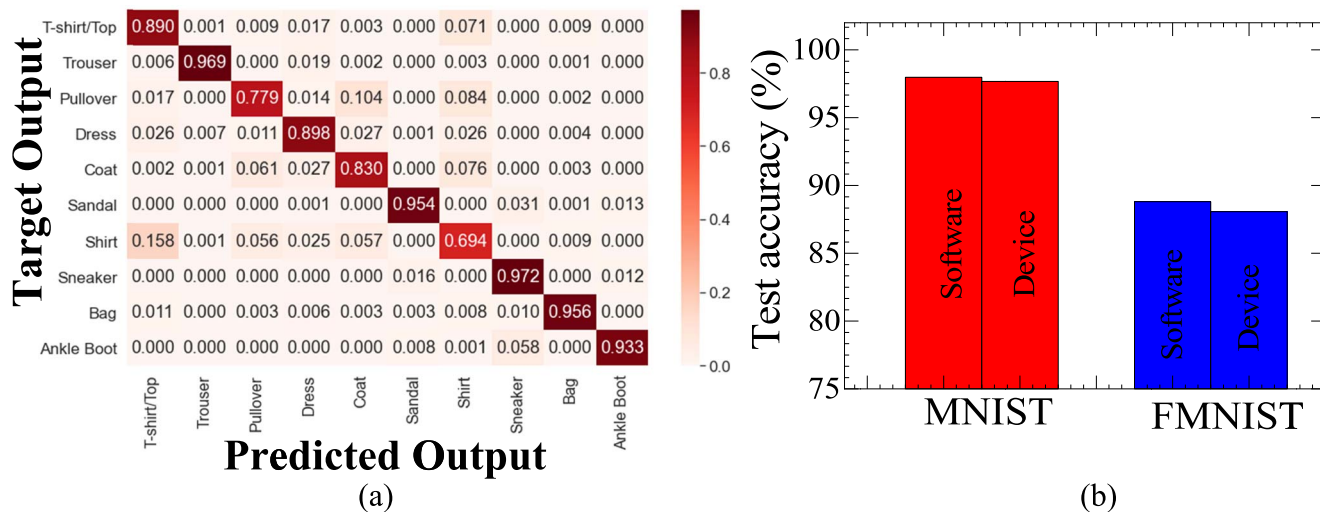


**Figure 6.** (a) Confusion matrix for the synaptic device  $\text{Ag}/\alpha\text{-Fe}_2\text{O}_3/\text{FTO}$  based ANN (b) Comparison of the pattern recognition accuracy (%) for both MNIST and FMNIST datasets. Both the software and device-based ANN performance are shown for better comparison.

predictions which match the target output label [54]. This shows the capability of the synaptic device-based ANN towards output class separability. Finally, we evaluated the performance of our synaptic device-based ANN on the popular Modified National Institute of Standards and Technology (MNIST) dataset to compare the performance of our synaptic device with previously published reports with a similar ANN configuration. From figure 6(b), we can confirm that the device based ANN reports a high recognition accuracy of 97.67% which is higher than previous reports [55], [56]. Such a high pattern recognition accuracy might be due to a combination of the synaptic device performance as well as the novel weight mapping strategy used in this report.

## Summary

In summary, we have investigated the analog bipolar resistive switching behaviour in  $\text{Ag}/\alpha\text{-Fe}_2\text{O}_3/\text{FTO}$  based RRAM device. The device showed stable and reproducible switching with good endurance and retentivity characteristics. Synaptic learning rules such as LTP, LTD and spike time dependent plasticity (STDP) behaviour are demonstrated. The proposed  $\alpha\text{-Fe}_2\text{O}_3$ -based RRAM device was successfully utilised as a synaptic element for pattern recognition task resulting in a high-test accuracy of 88.06% and 97.6% on the FMNIST and MNIST datasets respectively. The ideal device characteristics and high ANN performance showed that the fabricated device can be useful for practical ANN implementation.

## Acknowledgments

SNJ would like to thank the Indian Institute of Technology, Hyderabad and DST—SERB Core research Grant (CRG/2020/003497) for the financial support. PJ would like to thank CSIR-HRDG for the award of Senior Research


Fellowship (SRF). KUM would like to thank Gachon University for providing the necessary research support.

## Data availability statement

The data cannot be made publicly available upon publication because the cost of preparing, depositing and hosting the data would be prohibitive within the terms of this research project. The data that support the findings of this study are available upon reasonable request from the authors.

## ORCID iDs

Kannan Udaya Mohanan  <https://orcid.org/0000-0002-1270-4596>

S Narayana Jammalamadaka  <https://orcid.org/0000-0001-9235-7012>

## References

- [1] Hur J *et al* 2018 A recoverable synapse device using a three-dimensional silicon transistor *Adv. Funct. Mater.* **28** 1804844
- [2] Kim S, Choi B, Lim M, Kim Y, Kim H-D and Choi S-J 2018 Synaptic device network architecture with feature extraction for unsupervised image classification *Small* **14** 1800521
- [3] John R A, Ko J, Kulkarni M R, Tiwari N, Chien N A, Ing N G, Leong W L and Mathews N 2017 Flexible ionic-electronic hybrid oxide synaptic TFTs with programmable dynamic plasticity for brain-inspired neuromorphic computing *Small* **13** 1701193
- [4] Indiveri G and Liu S-C 2015 Memory and information processing in neuromorphic systems *Proc. IEEE* **103** 1379–97
- [5] Kuzum D, Yu S and Philip Wong H-S 2013 Synaptic electronics: materials, devices and applications *Nanotechnology* **24** 382001

- [6] Piccinini G 2004 The first computational theory of mind and brain: a close look at McCulloch and Pitts's 'logical calculus of ideas immanent in nervous activity' *Synthese* **141** 175–215
- [7] Christensen D V et al 2022 Roadmap on neuromorphic computing and engineering *Neuromorph. Comput. Eng.* **2** 022501
- [8] Spiga S 2020 *Memristive devices for Brain-Inspired Computing: from Materials, Devices, and Circuits to Applications: Computational Memory, Deep Learning, and Spiking Neural Networks* (Duxford: Woodhead Publishing)
- [9] Oh I, Pyo J and Kim S 2022 Resistive switching and synaptic characteristics in ZnO/TaON-Based RRAM for neuromorphic system *Nanomaterials* **12** 2185
- [10] Yu S, Wu Y, Jayasingh R, Kuzum D and Wong H-S P 2011 An electronic synapse device based on metal oxide resistive switching memory for neuromorphic computation *IEEE Trans. Electron Devices* **58** 2729–37
- [11] Covi E, Brivio S, Serb A, Prodromakis T, Fanciulli M and Spiga S 2016 Analog memristive synapse in spiking networks implementing unsupervised learning *Front. Neurosci.* **10** 1–13
- [12] Hong X, Loy D J, Dananjaya P A, Tan F, Ng C and Lew W 2018 Oxide-based RRAM materials for neuromorphic computing *J. Mater. Sci.* **53** 8720–46
- [13] Zahoor F, Azni Zulkifli T Z and Khanday F A 2020 Resistive random access memory (RRAM): an overview of materials, switching mechanism, performance, multilevel cell (mlc) storage, modeling, and applications *Nanoscale Res. Lett.* **15** 90
- [14] Hu S G, Liu Y, Chen T P, Liu Z, Yu Q, Deng L J, Yin Y and Hosaka S 2013 Emulating the Ebbinghaus forgetting curve of the human brain with a NiO-based memristor *Appl. Phys. Lett.* **103** 133701
- [15] Prezioso M, Merrih-Bayat F, Hoskins B D, Adam G C, Likharev K K and Strukov D B 2015 Training and operation of an integrated neuromorphic network based on metal-oxide memristors *Nature* **521** 61–4
- [16] Wang C, He W, Tong Y and Zhao R 2016 Investigation and manipulation of different analog behaviors of memristor as electronic synapse for neuromorphic applications *Sci. Rep.* **6** 22970
- [17] Chang T, Jo S-H and Lu W 2011 Short-term memory to long-term memory transition in a nanoscale memristor *ACS Nano* **5** 7669–76
- [18] Yao P et al 2017 Face classification using electronic synapses *Nat. Commun.* **8** 15199
- [19] Ielmini D and Wong H-S P 2018 In-memory computing with resistive switching devices *Nat. Electron.* **1** 333–43
- [20] Moon K, Lim S, Park J, Sung C, Oh S, Woo J, Lee J and Hwang H 2019 RRAM-based synapse devices for neuromorphic systems *Faraday Discuss.* **213** 421–51
- [21] Go J, Kim Y, Kwak M, Song J, Chekol S A, Kwon J-D and Hwang H 2019 W/WO<sub>3-x</sub> based three-terminal synapse device with linear conductance change and high on/off ratio for neuromorphic application *Appl. Phys. Express* **12** 026503
- [22] Milo V, Zambelli C, Olivo P, Pérez E K, Mahadevaiah M G, Ossorio O, Wenger C and Ielmini D 2019 Multilevel HfO<sub>2</sub>-based RRAM devices for low-power neuromorphic networks *APL Mater.* **7** 081120
- [23] Fang Y, Shi T, Zhang X, Wu Z, An J, Wei J, Lu J and Liu Q 2020 Impact of Ta/Ti electrodes on linearities of TaOx-based resistive random-access memories for neuromorphic computing *Sci. China Phys. Mech. Astron.* **63** 297311
- [24] Yang C-S, Shang D-S, Chai Y-S, Yan L-Q, Shen B-G and Sun Y 2017 Electrochemical-reaction-induced synaptic plasticity in MoO<sub>x</sub>-based solid state electrochemical cells *Phys. Chem. Chem. Phys.* **19** 4190–8
- [25] Wang Z Q, Xu H Y, Li X H, Yu H, Liu Y C and Zhu X J 2012 Synaptic learning and memory functions achieved using oxygen ion migration/diffusion in an amorphous InGaZnO memristor *Adv. Funct. Mater.* **22** 2759–65
- [26] Jetty P, Sahu D P and Jammalamadaka S 2022 Analog resistive switching in reduced graphene oxide and chitosan-based bio-resistive random access memory device for neuromorphic computing applications *Phys. Rapid Res. Lett.* **16** 2100465
- [27] Sahu D P and Jammalamadaka S N 2019 Detection of bovine serum albumin using hybrid TiO<sub>2</sub> + graphene oxide based Bio—resistive random access memory device *Sci. Rep.* **9** 16141
- [28] Sahu D P, Jetty P and Jammalamadaka S N 2021 Graphene oxide based synaptic memristor device for neuromorphic computing *Nanotechnology* **32** 155701
- [29] Wu W, Jiang C Z and Roy V A L 2016 Designed synthesis and surface engineering strategies of magnetic iron oxide nanoparticles for biomedical applications *Nanoscale* **8** 19421–74
- [30] Wu W, Changzhong Jiang C J and Roy V A L 2015 Recent progress in magnetic iron oxide–semiconductor composite nanomaterials as promising photocatalysts *Nanoscale* **7** 38–58
- [31] Yan X, Li Y, Zhao J, Xia Y, Zhang M and Liu Z 2015 Resistive switching model change induced by electroforming in  $\alpha$ -Fe<sub>2</sub>O<sub>3</sub> films *Phys. Lett. A* **379** 2392–5
- [32] Niu Y, Jiang K, Dong X, Zheng D, Liu B and Wang H 2021 High performance and low power consumption resistive random access memory with Ag/Fe<sub>2</sub>O<sub>3</sub> /Pt structure *Nanotechnology* **32** 505715
- [33] Wan X, Gao F, Lian X, Ji X, Hu E, He L, Tong Y and Guo Y 2018 Bio-mimicked atomic-layer-deposited iron oxide-based memristor with synaptic potentiation and depression functions *Jpn. J. Appl. Phys.* **57** 060303
- [34] Wang C, He W, Tong Y and Zhao R 2016 Investigation and manipulation of different analog behaviors of memristor as electronic synapse for neuromorphic applications *Sci. Rep.* **6** 22970
- [35] Yuan F-Y et al 2017 Conduction mechanism and improved endurance in HfO<sub>2</sub>-Based RRAM with nitridation treatment *Nanoscale Res. Lett.* **12** 574
- [36] Chen Y-C, Huang H-C, Lin C-Y, Hu S-T, Lin C-C and Lee J C 2019 Selectorless resistive switching memory: non-uniform dielectric architecture and seasoning effect for low power array applications *AIP Adv.* **9** 075119
- [37] Jung K, Kim Y, Im H, Kim H and Park B 2011 Leakage transport in the high-resistance state of a resistive-switching nbox thin film prepared by pulsed laser deposition *J. Korean Phy. Soc.* **59** 2778–81
- [38] Chen K-H, Tsai T-M, Cheng C-M, Huang S-J, Chang K-C, Liang S-P and Young T-F 2017 Schottky emission distance and barrier height properties of bipolar switching Gd:SiO<sub>x</sub> RRAM Devices under different oxygen concentration environments *Materials* **11** 43
- [39] Yen T-J, Chin A and Gritsenko V 2021 Improved device distribution in high-performance SiN<sub>x</sub> resistive random access memory via arsenic ion implantation *Nanomaterials* **11** 1401
- [40] Chiu F-C 2014 A review on conduction mechanisms in dielectric films *Adv. Mater. Sci. Eng.* **2014** 1–18
- [41] Lei X-Y, Liu H-X, Gao H-X, Yang H-N, Wang G-M, Long S-B, Ma X-H and Liu M 2014 Resistive switching characteristics of Ti/ZrO<sub>2</sub> /Pt RRAM device *Chin. Phys. B* **23** 117305
- [42] Voronkovskii V A, Aliev V S, Gerasimova A K and Islamov D R 2019 Conduction mechanisms of TaN/HfO<sub>x</sub> /Ni memristors *Mater. Res. Express* **6** 076411
- [43] Mondal S, Her J-L, Koyama K and Pan T-M 2014 Resistive switching behavior in Lu<sub>2</sub>O<sub>3</sub> thin film for advanced flexible memory applications *Nanoscale Res. Lett.* **9** 3

- [44] Liu C-F, Tang X-G, Wang L-Q, Tang H, Jiang Y-P, Liu Q-X, Li W-H and Tang Z-H 2019 Resistive switching characteristics of HfO<sub>2</sub> thin films on mica substrates prepared by sol-gel process *Nanomaterials* **9** 1124
- [45] Sahu D P and Jammalamadaka S N 2017 Remote control of resistive switching in TiO<sub>2</sub> based resistive random access memory device *Sci. Rep.* **7** 17224
- [46] Ilyas N, Li D, Li C, Jiang X, Jiang Y and Li W 2020 Analog switching and artificial synaptic behavior of Ag/SiO<sub>x</sub>:Ag/TiO<sub>x</sub>/p++-Si memristor device *Nanoscale Res. Lett.* **15** 30
- [47] Wang T-Y, He Z-Y, Chen L, Zhu H, Sun Q-Q, Ding S-J, Zhou P and Zhang D 2018 An organic flexible artificial biosynapses with long-term plasticity for neuromorphic computing *Micromachines* **9** 239
- [48] Xiao H, Rasul K and Vollgraf R 2017 Fashion-MNIST: a novel image dataset for benchmarking machine learning algorithms 1–6 *arXiv* 1708.07747
- [49] Udaya Mohanan K, Cho S and Park B-G 2022 Medium-temperature-oxidized geox resistive-switching random-access memory and its applicability in processing-in-memory computing *Nanoscale Res. Lett.* **17** 63
- [50] Paszke A *et al* 2019 Advances in Neural Information Processing Systems 8024–35 ([https://papers.nips.cc/paper\\_files/paper/2019/hash/bdbca288fee7f92f2bfa9f7012727740-Abstract.html](https://papers.nips.cc/paper_files/paper/2019/hash/bdbca288fee7f92f2bfa9f7012727740-Abstract.html))
- [51] Ruder S 2016 an overview of gradient descent optimization algorithms *arXiv* 1609.04747 1–14
- [52] Joshi V, Le Gallo M, Haefeli S, Boybat I, Nandakumar S R, Piveteau C, Dazzi M, Rajendran B, Sebastian A and Eleftheriou E 2020 Accurate deep neural network inference using computational phase-change memory *Nat. Commun.* **11** 2473
- [53] Wang K, Liu Z, Lin Y, Lin J and Han S 2018 8612–20 HAQ: Hardware-Aware Automated Quantization with Mixed Precision *Proceedings of the IEEE/CVF Conference on Computer Vision and Pattern Recognition (CVPR)* ([https://openaccess.thecvf.com/content\\_CVPR\\_2019/html/Wang\\_HAQ\\_Hardware-Aware\\_Automated\\_Quantization\\_With\\_Mixed\\_Precision\\_CVPR\\_2019\\_paper.html](https://openaccess.thecvf.com/content_CVPR_2019/html/Wang_HAQ_Hardware-Aware_Automated_Quantization_With_Mixed_Precision_CVPR_2019_paper.html))
- [54] Udaya Mohanan K, Cho S and Park B-G 2023 Optimization of the structural complexity of artificial neural network for hardware-driven neuromorphic computing application *Appl. Intell.* **53** 6288–306
- [55] Kim S K *et al* 2020 3D stackable synaptic transistor for 3D integrated artificial neural networks *ACS Appl. Mater. Interfaces* **12** 7372–80
- [56] Kim D *et al* 2020 Pd/IGZO/p<sup>+</sup>-Si synaptic device with self-graded oxygen concentrations for highly linear weight adjustability and improved energy efficiency *ACS Appl. Electron. Mater.* **2** 2390–7